RESEARCH ARTICLE
PLANETARY SCIENCES

Earth and Planetary Physics
9: 879–890, 2025
doi: 10.26464/epp2025074

Petrogenesis of the gabbroic shergottite Northwest Africa 12241: Insights into the common intrusive process of shergottites

YunHua Wu[1], Pan Yan[1], Qing Pan[1], and ZhiYong Xiao[1,2*]

[1]Planetary Environmental and Astrobiological Research Laboratory, School of Atmospheric Sciences, Sun Yat-sen University, Zhuhai 519082, China;

[2]Center for Excellence in Comparative Planetology, Chinese Academy of Sciences, Hefei 230026, China

Key Points:

- Northwest Africa 12241 is an olivine gabbroic shergottite derived from an intermediate source reservoir.
- Ponding and crystallization at depth, followed by subsequent ascent and emplacement of melt and mush, is a common process on Mars.
- Staging chambers with varying compositions are pervasive at the crust–mantle boundary.

Citation: Wu, Y. H., Yan, P., Pan, Q., and Xiao, Z. Y. (2025). Petrogenesis of the gabbroic shergottite Northwest Africa 12241: Insights into the common intrusive process of shergottites. *Earth Planet. Phys.*, *9*(4), 879–890. http://doi.org/10.26464/epp2025074

Abstract: Gabbroic and poikilitic shergottites are intrusive igneous rocks on Mars, providing significant insights into the igneous processes within the Martian crust. However, questions remain regarding the chemical signatures of their source reservoirs and the petrogenetic links among shergottites of different subtypes. In this study, we present petrological and mineralogical analyses of the intermediate shergottite Northwest Africa (NWA) 12241. Quantitative textural analysis and pyroxene chemistry indicate that, despite minor differences such as the accumulation of intermediate-sized olivine and smaller pyroxene oikocrysts, NWA 12241 has experienced a similar emplacement history as typical poikilitic and gabbroic shergottites. The estimated parent melt of NWA 12241 is consistent with derivation from an intermediate source reservoir, resulting from the mixing of enriched and depleted mantle end-members at depth, prior to magma ascent. Similar emplacement histories of variable poikilitic and gabbroic shergottites suggest the common presence of multiple staging magma chambers with different compositions at the crust–mantle boundary, coupled with prolonged ponding at this depth. Our study highlights that, in addition to magma mixing and assimilation, magmatic differentiation and cooling conditions at shallow depths are crucial processes leading to textural and compositional variations among shergottites of different subtypes.

Keywords: Martian shergottite; olivine gabbroic shergottite; magma emplacement; mantle reservoir

1. Introduction

Martian meteorites, as the only samples currently available from Mars, provide crucial records of the chemical signatures and geological history of the planet. With the exception of the breccia Northwest Africa (NWA) 7034 and its pairings, most Martian meteorites are of igneous origin and can be classified into four categories: shergottites, nakhlites (clinopyroxenites), chassignites (dunites), and orthopyroxenites (Papike et al., 2009). Shergottites, which are the most common type, exhibit a variety of petrological and geochemical characteristics. They are further subdivided into olivine-phyric, basaltic, poikilitic, and gabbroic shergottites based on their petrological textures (McSween and Treiman, 1998; Goodrich, 2002; Papike et al., 2009; Udry et al., 2017). Olivine-phyric and basaltic shergottites are suggested to represent extrusive or hypabyssal volcanic products, whereas poikilitic and gabbroic shergottites are believed to have an intrusive origin formed at greater depths (Udry et al., 2020). Moreover, shergottites can be divided into enriched, intermediate, and depleted groups based on the relative abundance of light rare earth elements (LREEs; Papike et al., 2009). The diverse petrological and chemical characteristics of these meteorites provide valuable insights into the chemical evolution and magmatic processes of Mars from the deep mantle to the shallow surface.

Given the large abundance of intrusive rocks on Earth, the Martian crust is also expected to contain a substantial amount of intrusive rock (Filiberto et al., 2014). However, the current collection of Martian meteorites is predominantly composed of extrusive and hypabyssal samples. Nevertheless, petrographic characteristics, along with major and trace element compositions, indicate that samples from different petrological subgroups may be closely related. A notable example is the gradational petrological transition between olivine-phyric and basaltic lithologies observed in Elephant Moraine A79001 (EETA 79001), which is proposed to reflect a primary igneous feature resulting from the emplacement of magma containing entrained crystals, followed by differentiation through crystal settling and *in situ* crystallization (Van Niekerk

First author: Y. H. Wu, wuyh76@mail.sysu.edu.cn
Correspondence to: Z. Y. Xiao, xiaozhiyong@mail.sysu.edu.cn
Received 12 JAN 2025; Accepted 03 APR 2025.
First Published online 30 MAY 2025.

et al., 2007). Moreover, the similar phosphorus zoning pattern of olivine megacrysts suggests that the intermediate poikilitic shergottite NWA 11065 and the intermediate olivine-phyric shergottite NWA 6234 may have crystallized from the same magmatic plumbing system (Gross et al., 2013a; Rahib et al., 2019). Investigating the formation scenario of intrusive samples and the petrogenetic relationships among samples of different petrological subgroups could provide vital information on the lithological diversity of the Martian crust.

Most poikilitic and gabbroic samples are enriched and intermediate in LREE composition (e.g., Howarth et al., 2014; Rahib et al., 2019; Benaroya et al., 2024), with only one depleted sample, Asuka 12325 (Takenouchi et al., 2023). The similar isotopic compositions (e.g., ^{146,147}Sm-^{142,143}Nd, ^{176}Lu-^{176}Hf) of samples within the same geochemical subtype, despite differences in their petrological subtypes, indicate that they may originate from a similar mantle reservoir. For example, the similar ^{176}Lu-^{176}Hf compositions of the enriched poikilitic shergottite NWA 10169 and the enriched olivine-phyric shergottite Larkman Nunatak (LAR) 06319 indicate origination from a similar source reservoir (Shafer et al., 2010; Combs et al., 2019). Moreover, samples with similar geochemical subtypes tend to have similar ejection ages, indicating that they were likely ejected from the same source crater on the Martian surface (Wieler et al., 2016). This similarity also implies a close spatial relationship among samples from the same geochemical groups (Wieler et al., 2016; Lapen et al., 2017). The formation of enriched and depleted mantle reservoirs on Mars may be related to early differentiation processes (Brandon et al., 2012; Armytage et al., 2018). However, the timing of the formation of intermediate source reservoirs is not well constrained. The reservoirs could have formed through various processes, such as mixing during or prior to the melting of mantle sources, or by assimilation of crustal materials (Herd et al., 2002; Treiman and Filiberto, 2015).

The Martian shergottite NWA 12241, with a total mass of 1150 g, has been classified in the Meteoritical Bulletin as an olivine gabbroic shergottite with an orthocumulate texture (Gattacceca et al., 2020). Its Nd-Hf isotopic compositions suggest origination from an intermediate mantle source (Lapen et al., 2019), making it an ideal target for investigating the chemical signatures and formation of intermediate source reservoirs. Notably, this sample contains birefringent plagioclase (Gattacceca et al., 2020) instead of the amorphous plagioclase commonly observed in most shergottites (Papike et al., 2009), thus potentially originating from a different location. Therefore, NWA 12241 was selected for detailed analyses of textural features and mineral chemistry to investigate its formation conditions, its emplacement history, and the geochemical signatures of its source reservoir. This study aims to elucidate the relationship between NWA 12241 and other Martian shergottites of different petrological and geochemical subtypes, as well as to shed light on the related geological processes. Our findings highlight the significant role of magmatic differentiation and cooling conditions under shallow circumstances in shaping the petrological and mineralogical diversity of Martian intrusive rocks.

2. Materials and Methods

The fragment of NWA 12241 was cut, embedded in epoxy resin, and then polished for petrological and mineralogical analyses. Scanning electron microscopy (SEM) observations were performed using a ZEISS Sigma 300 instrument at the Southern Marine Science and Engineering Guangdong Laboratory (Zhuhai). Elemental mapping was carried out with a TESCAN Integrated Mineral Analyzer (TIMA), which was operated at an acceleration voltage of 25 kV and a probe current of 9 nA at the Nanjing Hongchuang Geological Exploration Technology Service Co., Ltd. The working distance was set to 15 mm. Pixel spacing was set to 2 μm, and dot spacing was set to 6 μm. The current and backscattered electron (BSE) signal intensity were calibrated on a platinum Faraday cup by using the automated procedure.

Backscattered electron images were digitized using ImageJ software to determine grain shape parameters, including length, width, orientation, and area. Grain boundaries were identified on BSE images manually with the aid of X-ray elemental maps. The mineral modal abundance was estimated by quantifying the area of an individual phase relative to the total area measured by ImageJ. The crystal size distribution (CSD) of minerals was analyzed to elucidate the dynamics during crystallization (Higgins, 2000; Lentze and McSween, 2000). The measured length and width of crystals were processed using the spreadsheet CSDslice to acquire the best matching long, intermediate, and short axes (Morgan and Jerram, 2006). These parameters, in addition to the grain shape measurements by ImageJ, were then input into CSDCorrections software to analyze the relationship between population density and crystal size. The spatial distribution patterns of minerals were evaluated based on the big-*R* value, which quantifies the spatial distribution pattern, as calculated by CSDCorrections and the corresponding porosity (modal abundance of other phases; Jerram et al., 1996, 2003).

Raman spectra of minerals were acquired with a Thermo micro-Raman spectrometer at the Purple Mountain Observatory, Chinese Academy of Sciences, to analyze potential phase transitions. Spectra were acquired using a 532 nm unpolarized laser with a power of 3 mW. The total analytical time was 60 s. The estimated spot size was 1.1 μm, and the spectral resolution was 1 to 2 cm^{-1}.

Major and minor elements of minerals were determined with a JEOL JXA-iSP100 Electron Probe Microanalyzer (EPMA). The accelerating voltage was 15 kV, and the probe current was 20 nA for olivine and pyroxene, 10 nA for plagioclase, 5 nA for phosphates, and 50 nA for spinel group minerals. Detection limits were better than 0.05 wt% for most elements and better than 0.1 wt% when analyzing phosphates. All data were corrected using the ZAF (Z, atomic number; A, absorption; F, fluorescence) correction method for matrix effect. Oxygen fugacity was estimated by analyzing the major element compositions of coexisting olivine and spinel. The calculation was performed using the Excel spreadsheet developed in the work of Nikolaev et al. (2016).

In situ trace element analysis of minerals was conducted using LA-ICP-MS (laser ablation–inductively coupled plasma–mass spectrometry). The RESOlution-SE model laser ablation system (Applied Spectra, USA) was equipped with an ATLEX 300 Excimer Laser (ATL Lasertechnik GmbH, Germany) and a dual-volume S155 ablation cell. The laser ablation system was coupled with an Agilent 7900 ICP-MS instrument. Detailed tuning parameters were

the same as described by Thompson et al. (2018). The analyzed spot size was 50 μm for silicates (10 Hz with a fluence of 4 J/cm^2) and 38 μm for phosphates (5 Hz with a fluence of 3 J/cm^2). National Institute of Standards and Technology (NIST) Standard Reference Material (SRM) 610 was used as primary reference material. U.S. Geological Survey Geochemical Reference Materials BCR-2G and BIR-1G were used as secondary reference materials. Triplets of reference materials were bracketed between multiple groups of 10 to 12 sample unknowns. For silicates, ^{29}Si was used as the internal standard element to calibrate trace element concentrations. For phosphates, NIST 610 and ^{43}Ca were used as the external reference material and internal standard element, respectively, to calibrate the trace element concentrations. The major and trace element analyses described above were conducted at the Nanjing Hongchuang Geological Exploration Technology Service Co., Ltd. The bulk major and trace element compositions were estimated based on the average concentrations of each mineral with their respective mineral modal abundances.

3. Results

3.1 Petrology

The major silicate phases in NWA 12241 are olivine, pyroxene, and plagioclase, with minor phases that include apatite, chromite, ilmenite, troilite, and metal (Figures 1a and S1a). Euhedral to subhedral olivine is the dominant phase, with grain sizes ranging from tens of microns to 1.4 mm in length (Figure S1b). Pyroxene is less abundant, with grains ranging up to 2.0 mm in length. Notably, coarse pyroxene may poikilitically enclose olivine and chromite of varying sizes. Olivine chadacrysts are typically rounded or irregular in shape (Figure 1b). In some cases, pyroxene does not enclose olivine chadacrysts in the cores (Figure 1c).

Plagioclase generally occurs as laths or anhedral grains, interstitially presenting between olivine and pyroxene. It is only partially transformed into an amorphous phase, which appears smooth in BSE images (Figure 1d). The amorphous characteristic of these plagioclases is supported by the broad bumps observed in the Raman spectra (Figure S2). Chromite generally presents as small inclusions (up to 260 μm in length) within olivine and pyroxene. Apatite and merrillite occur as subhedral grains or in intergrowths with irregular boundaries between apatite and merrillite (Figure 1e). Minor iron oxide has been observed near the boundaries. The texture and assemblage are similar to those formed during fluid interaction observed in shergottites (Gross et al., 2013b; Wu YH et al., 2024). Melt pockets are characterized by the presence of melted silicates and droplets of opaque phases (Figure 1f).

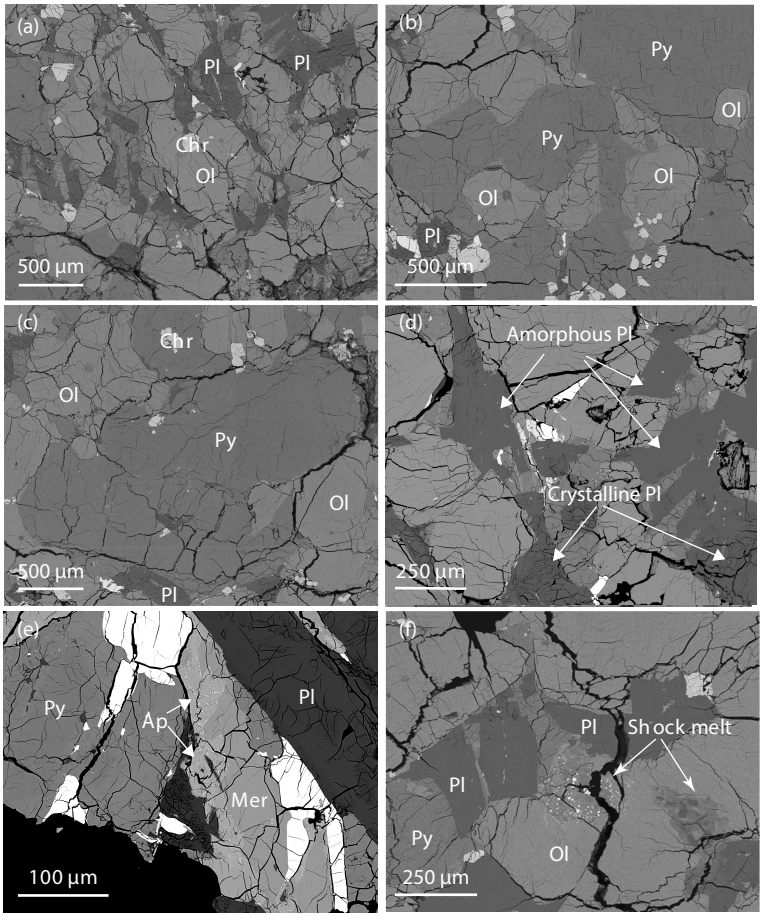

Figure 1. Backscattered electron (BSE) images of NWA 12241. (a) Sample composed predominantly of olivine, with lesser amounts of pyroxene and plagioclase. (b) Olivine poikilitically enclosed in pyroxene. (c) Coarse pyroxene without olivine inclusions. (d) Amorphous plagioclase and crystalline plagioclase with fractures. (e) Coexisting apatite and merrillite. (f) Impact melt pockets. Ap, apatite; Chr, chromite; Mer, merrillite; Ol, olivine; Pl, plagioclase; Py, pyroxene.

The modal abundances of minerals are as follows (vol%): olivine, 53.4; pyroxene, 31.7 (orthopyroxene, 0.3; low-Ca pyroxene, 11.0; high-Ca pyroxene, 20.4); plagioclase, 11.4; feldspathic mesostasis, 0.1; chromite, 1.3; ilmenite, 0.4; phosphate, 1.4; troilite and metal, 0.3. Elemental mapping (Figures 2a–2b) indicated that olivine typically exhibits limited chemical variation. Larger (millimeter-sized) pyroxene grains have low-Ca pyroxene cores with Ca-rich rims or patches (Figures 2c–2d and S1c). The relatively high abundance of olivine and the low abundance of plagioclase fall within the range observed in typical poikilitic shergottites (Rahib et al., 2019).

3.2 Quantitative Textural Analysis

A quantitative textural analysis of silicates was conducted to constrain the dynamics of crystal nucleation and growth (Lentze and McSween, 2000). The olivine CSD profile exhibits a downturn at the smallest grain size bins, similar to those observed in typical poikilitic and gabbroic shergottites (Figure 3a). However, NWA 12241 exhibits a slightly higher population density for grains in the intermediate size range (1.0–2.0 mm). The linear regression of all olivine grains yields a slope of −2.5 with an intercept of 3.9, whereas olivine grains poikilitically enclosed in pyroxene exhibit a steeper slope of −2.9 and an intercept of 3.0. Moreover, olivine grains larger than 0.1 mm reveal a slope of −2.5.

The CSD profile of pyroxene also shows a downturn at the smallest size bins, similar to olivine. However, larger pyroxene grains exhibit a relatively linear correlation, with a subtle upturn observed at the largest grain size bins (Figure 3b). The overall pyroxene population exhibits a slope of −2.7 with an intercept of 3.4. Notably, pyroxene grains in the larger size bins display a flatter slope compared with olivine. For instance, for grains larger than 0.6 mm in length, the slopes are −1.71 for pyroxene and −3.36 for olivine.

The spatial distribution pattern, as indicated by the big-*R* value and the modal abundances of olivine and pyroxene, suggests a clustered touching framework characteristic of intrusive rocks (Figures 3c–3d; Jerram et al., 2003). The alignment factor, which ranges from 0 for massive rocks to 1 for oriented rocks, was applied to evaluate the fabric quality. The alignment factors of olivine and pyroxene are 0.12 and 0.13, respectively. The alignment factor of plagioclase, which reflects the spatial relationships of interstitial spaces between olivine and pyroxene, is significantly low, at 0.05. These results suggest the absence of a preferred orientation in the silicates of NWA 12241. Although grain boundaries are challenging to identify because of effects such as textural equilibration during crystallization and shock metamorphism, the overall trend remains noteworthy.

3.3 Chemical Composition

3.3.1 Whole rock

The measured and calculated major and trace element compositions are listed in Tables S1 and S2, respectively. The bulk major element composition was calculated based on the average compositions of olivine, low-Ca pyroxene, high-Ca pyroxene, plagioclase, and spinel, with their total modal abundances normalized to 100 vol%. In addition, the bulk trace element abundance was determined using the average compositions of olivine, low-Ca pyroxene, high-Ca pyroxene, plagioclase, and phosphate, without normalizing their total modal abundances to 100 vol%. The calculated bulk Mg# (molar Mg/[Mg + Fe] × 100 = 57.8) and CaO (4.21 wt%) are consistent with a permafic composition (Figure 4a; Irving et al., 2010). The relatively high MgO content and low K content of NWA 12241 is within the range observed in

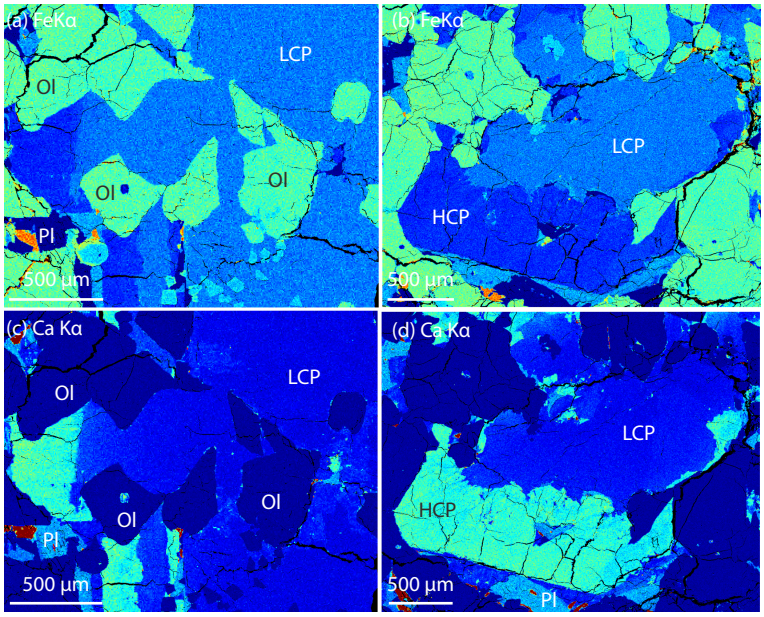

Figure 2. Elemental maps of Fe and Ca in the regions shown in Figures 1b and 1c. (a, b) Fe elemental maps showing limited chemical variations of olivine. (c, d) Ca elemental maps showing patches and rims of high-Ca pyroxene (HCP) associated with low-Ca pyroxene (LCP). The scale bar is 500 μm in length.

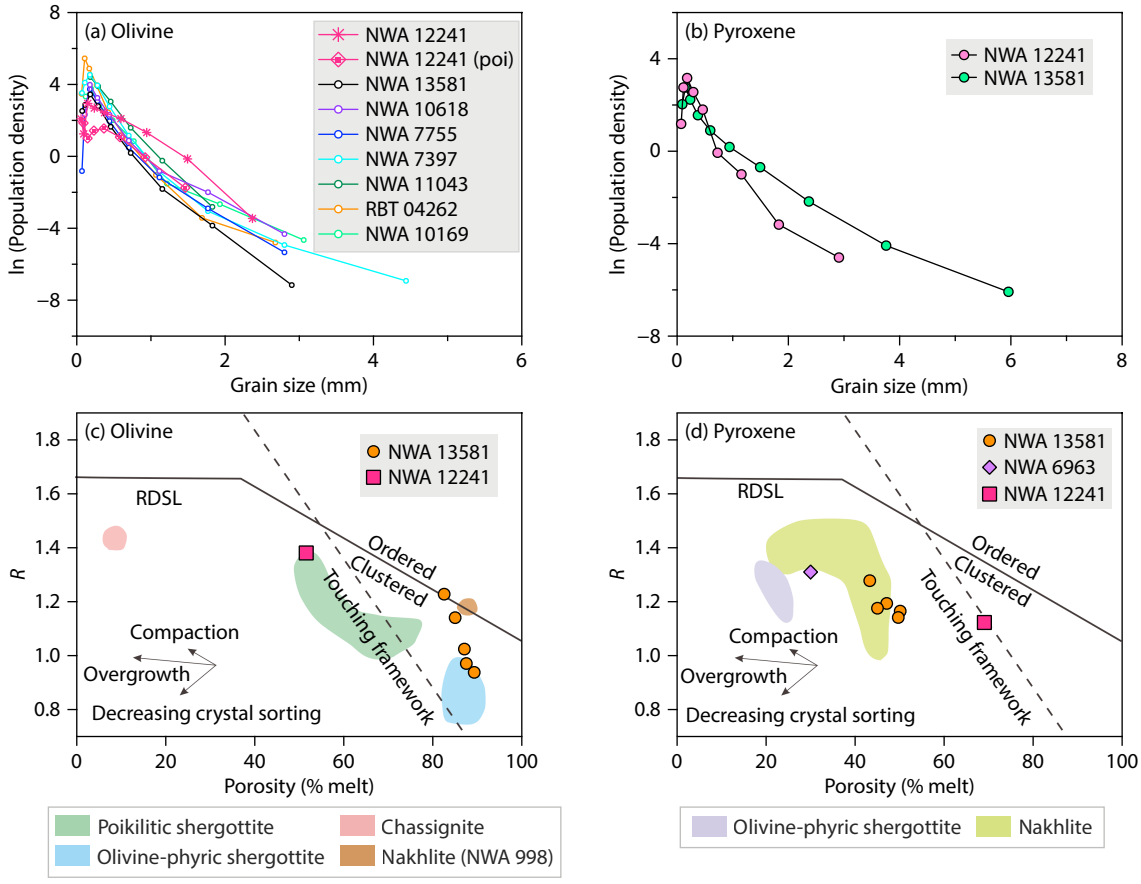

Figure 3. Quantitative textural analysis results for olivine and pyroxene in NWA 12241. (a) Crystal size distribution (CSD) profiles for olivine in NWA 12241 compared with gabbroic (Wu YH et al., 2023) and poikilitic shergottites such as NWA 10618 and Roberts Massif (RBT) 04262 (Rahib et al., 2019). NWA 12241 (poi) refers to olivine in the poikilitic region. (b) CSD profiles for pyroxene compared with gabbroic shergottite NWA 13581 (Wu YH et al., 2023). (c) Spatial distribution patterns of olivine compared with poikilitic shergottites (Rahib et al., 2019), olivine-phyric shergottites (Basu Sarbadhikari et al., 2009; Ennis and McSween, 2014), chassignite and nakhlite (Udry and Day, 2018), and gabbroic NWA 13581 (Wu YH et al., 2023). (d) Spatial distribution patterns of pyroxene compared with olivine-phyric shergottites (Ennis and McSween, 2014), nakhlite (Udry and Day, 2018), NWA 6963 (Filiberto et al., 2018), and NWA 13581 (Wu YH et al., 2023). The boundaries of the touching framework and RSDL (random sphere distribution line) are from Jerram et al. (2003). The *R* values, calculated via the CSDCorrections software, quantify spatial distribution patterns by comparing observed crystal distribution to a random distribution.

gabbroic, poikilitic, and olivine phyric shergottites (Figures 4b–4c).

The high Mg# value and Ni content of NWA 12241 are comparable to those of enriched gabbroic, enriched poikilitic, and both enriched and depleted olivine-phyric shergottites (Figure 4d). But its low La and Zr contents are within the range observed in intermediate poikilitic and depleted olivine-phyric shergottites (Figures 4e–4f). The bulk REE concentrations with a $(La/Yb)_{CN}$ value (where the subscript CN represents abundance normalized to CI-chondrite) of 0.4 place NWA 12241 in an intermediate category (Figure 5a; Papike et al., 2009). The Eu content does not exhibit a significant anomaly, with an Eu_{CN}/Eu^* value of 1.1 (where $Eu^* = 0.5 \times [Sm + Gd]_{CN}$).

3.3.2 Minerals

Olivine exhibits a relatively limited chemical variation, with Mg# values varying from 61.6 to 68.5 (average Mg# = 65.9, FeO/MnO = 43.4–50.9). Chemical zoning within individual olivine grains is not evident, with only a few large (e.g., millimeter-sized) grains displaying subtle variations. The abundance of LREEs in olivine is negligible ($Lu \leq 0.02$ ppm; Figure 5b). The compositions of amorphous plagioclase ($An_{53.4–55.6}Ab_{43.3–45.6}Or_{1.0–1.3}$) and crystalline plagioclase ($An_{49.3–56.0}Ab_{42.7–48.7}Or_{1.1–2.0}$) overlap, with no significant chemical difference. Both phases exhibit positive Eu anomalies, with LREEs slightly more enriched relative to HREEs (heavy rare earth elements; Figure 5b).

Pyroxene is dominated by high-Ca pyroxene ($Fs_{16.1–20.5}Wo_{28.4–38.6}$, FeO/MnO = 21.0–29.0) and a lesser amount of low-Ca pyroxene ($Fs_{21.3–32.6}Wo_{5.9–24.1}$, FeO/MnO = 24.2–33.7). Both exhibit limited chemical variation, with Mg# values varying from 63.4 to 74.7 (average = 71.2). The Ti/Al ratios are mostly low, ranging from 0.07 to 0.18, with a few ranging up to 0.53. Pyroxene is LREE depleted ($[La/Yb]_{CN} \leq 0.1$), with Yb concentrations ranging from 0.17 to 0.71 ppm (Figure 5c). A subset of low-Ca pyroxene exhibits a negative Eu anomaly, with Eu_{CN}/Eu^* values ranging from 0.5 to 0.6. The remaining pyroxene grains show a less pronounced Eu anomaly, with Eu_{CN}/Eu^* values between 0.7 and 0.9. Phosphates, dominated by apatite and merrillite, are the major REE carriers

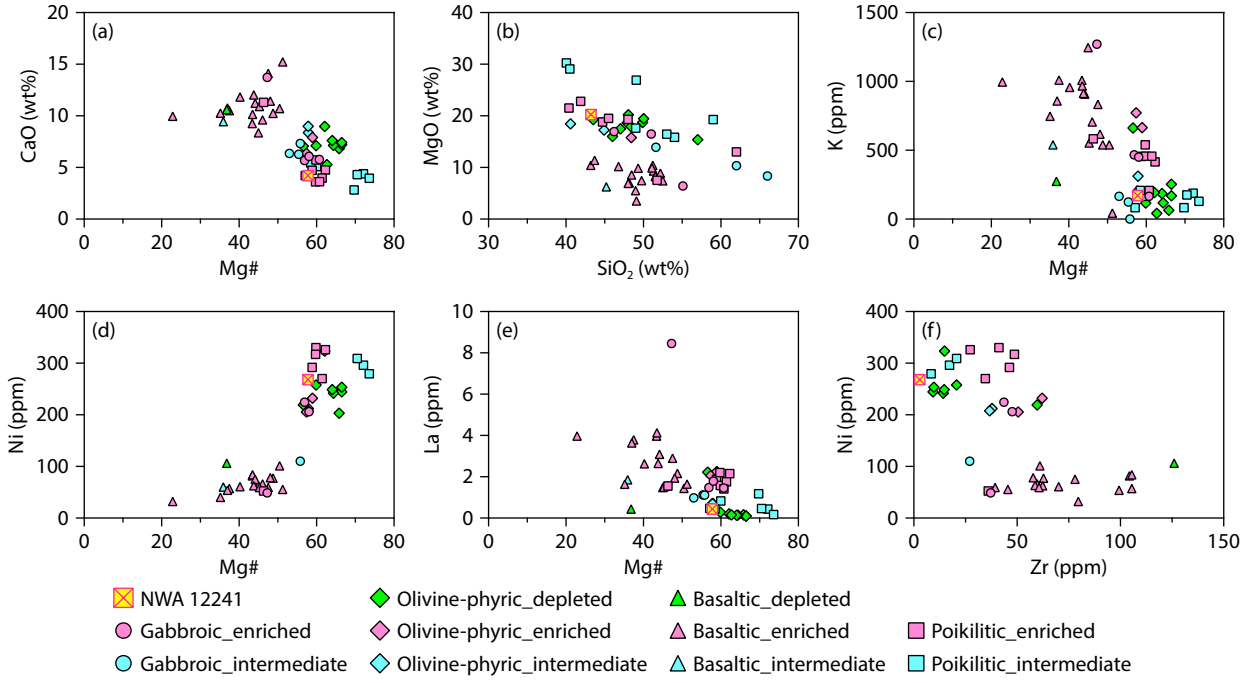

Figure 4. Bulk major and minor element compositions of NWA 12241 compared with shergottites. (a) Mg# versus CaO; (b) SiO_2 versus MgO; (c) Mg# versus K; (d) Mg# versus Ni; (e) Mg# versus La; (f) Zr versus Ni. Data sources: Barrat et al. (2001, 2002); Jambon et al. (2002); Kring et al. (2003); Shirai and Ebihara (2004); Irving et al. (2011); Filiberto et al. (2012); Udry et al. (2017); Day et al. (2018); Irving et al. (2018); Combs et al. (2019); Rahib et al. (2019).

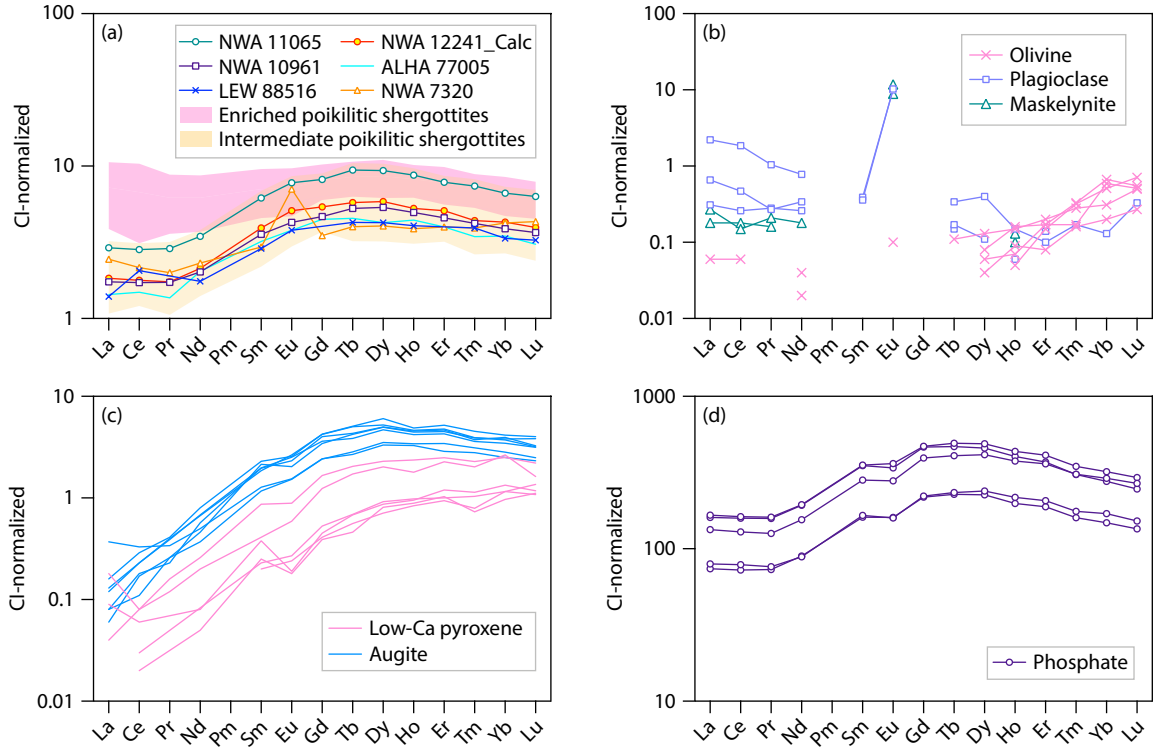

Figure 5. Rare earth element (REE) compositions of bulk rock and minerals of NWA 12241. (a) Calculated bulk REE of NWA 12241 compared with intermediate poikilitic shergottite NWA 11065 (Rahib et al., 2019), NWA 10961 (Rahib et al., 2019), Allan Hills (ALH) A77005 (Lodders, 1998), Lewis Cliff (LEW) 88516 (Lodders, 1998), and the gabbroic shergottite NWA 7320 (Udry et al., 2017). The regions for intermediate and enriched poikilitic shergottites are shown in yellow and pink, respectively. REE of minerals including (b) olivine, plagioclase, and maskelynite, (c) pyroxene, and (d) phosphate.

showing a relative depletion in LREE, with an average $(La/Yb)_{CN}$ value of 0.5 (Figure 5d).

4. Discussion

4.1 Classification of NWA 12241

With the growing number and diversity of identified Martian intrusive meteorites, the current classification scheme has become somewhat ambiguous. Although poikilitic shergottites belong to gabbroic or lherzolitic lithologies (Rahib et al., 2019), recently identified olivine gabbroic samples (e.g., NWA 13227; Benaroya et al., 2024) exhibit both similarities with and differences from typical poikilitic shergottites. The similarities include the presence of olivine chadacrysts enclosed in pyroxene, whereas the differences include the scarcity of large pyroxene oikocrysts and a more varied mineral composition in some cases, such as the CaO content in pyroxene (Wu YH et al., 2023; Benaroya et al., 2024). In most cases, poikilitic shergottites are characterized by a bimodal texture with large pyroxene oikocrysts from 3 to 10 mm in length, and gabbroic shergottites are characterized by a cumulate texture with millimeter-sized phenocrysts up to 5.0 mm (Udry et al., 2020).

Northwest Africa 12241 is classified as an olivine gabbroic shergottite in the Meteoritical Bulletin (Gattacceca et al., 2020), but it has also been referred to as a poikilitic shergottite in some studies (e.g., Nicklas et al., 2021). The olivine abundance in NWA 12241 is higher than that in currently identified olivine gabbroic shergottites, which are reported to be variable (e.g., NWA 13227: 26%, Benaroya et al., 2024; NWA 11509: 17.1%, Irving et al., 2018; NWA 13581: 15.6%, Wu YH et al., 2023) and to fall within the upper range of poikilitic shergottites (Rahib et al., 2019, and references therein). However, the smaller pyroxene oikocrysts and lesser amount of enclosed olivine chadacrysts differ from typical poikilitic shergottites, indicating differences in formation conditions. Therefore, NWA 12241 is classified as an olivine gabbroic shergottite to distinguish potential differences in crystallization dynamics from those of typical poikilitic shergottites. The similarities with and differences from typical poikilitic shergottites imply a close petrogenetic link and diversity in the crystallization dynamics of Martian intrusive magmatism.

4.2 Crystallization Condition

Experimental studies have established correlations between the Ti/Al ratios of pyroxene and pressure (Nekvasil et al., 2004; Filiberto et al., 2010). A Ti/Al ratio ranging from 0.1 to 0.2 in most NWA 12241 pyroxene is consistent with crystallization at pressures around 9.3 kbar (Nekvasil et al., 2004; Filiberto et al., 2010), which corresponds to a depth of approximately 85 km in the lower crust or the upper mantle (Zuber et al., 2000; Filiberto and Dasgupta, 2015). The relatively limited variation in the Ti/Al ratio observed in most pyroxene grains, including some in nonpoikilitic regions, along with subtle variations in the major element composition of silicates, suggests that the majority of these pyroxene cores likely formed at depth.

Assuming a temperature of 1000°C and a pressure of 9.3 kbar, the chemical compositions of coexisting olivine and chromite reveal oxygen frugalities ranging from QFM (quartz–fayalite–magnetite buffer) −3.9 to −2.8 for poikilitically enclosed olivine and from QFM −2.9 to −2.3 for other olivine (Nikolaev et al., 2016). These variations in oxygen fugacity span over one log unit of QFM, with more oxidized conditions occurring during the late stage of crystallization. The oxygen fugacity values are comparable to those of intermediate shergottites and the early-formed regions of several enriched poikilitic and gabbroic shergottites, such as Lewis Cliff (LEW) 88516, NWA 10961, and Allan Hills (ALH) A77005 (Rahib et al., 2019). Moreover, these values are slightly more reduced than those of enriched basaltic shergottites, such as NWA 5298 (Hui HJ et al., 2011) and Shergotty (Herd et al., 2001).

The oxygen fugacity in magmatic systems can change as a result of several processes, including progressive crystallization (autooxidation), degassing, decompression during magma ascent, fluid interaction, and mixing or assimilation with oxidized materials (Goodrich et al., 2003; Herd, 2003; Peslier et al., 2010; Balta et al., 2013; Castle and Herd, 2017; Combs et al., 2019; Wu YH et al., 2024). In Martian intrusive rocks such as poikilitic shergottites, the increase in oxygen fugacity can be as large as three orders of magnitude (Rahib et al., 2019). In the case of NWA 12241, the closed system confined in terms of REE abundances, excluding the possibility of the influence of mixing or assimilation with chemically distinct components. Although the extent of degassing is not firmly constrained, an increase of one log unit in oxygen fugacity could be readily achieved through autooxidation during magma ascent and late-stage crystallization (Peslier et al., 2010; Castle and Herd, 2017).

4.3 Parent Melt Composition

The compositions of melts in equilibrium with silicates were evaluated using element partition coefficients to understand the chemical signatures of the source reservoir and chemical evolution during the formation of NWA 12241 (Table S3). Specifically, the Fe-Mg partition coefficient for olivine is 0.35 (Filiberto and Dasgupta, 2011), whereas for pyroxene, the coefficient is estimated as 0.27, calculated based on the average Mg# of early-formed pyroxene (72.6) following the method of Bédard (2010). Moreover, the REE partition coefficients for pyroxene were calculated based on the average compositions of pigeonite and high-Ca pyroxene (Sun CG and Liang Y, 2012, 2013; Yao LJ et al., 2012).

The Mg-rich olivine (Mg# = 68.5) and pyroxene (Mg# = 74.7) in NWA 12241 indicate that their parent melts had similar Mg# values around 43–44, which is lower than the bulk Mg# of NWA 12241. However, the calculated REE abundance of the parent melts in equilibrium with early-formed pyroxene (both Mg-rich low-Ca and high-Ca pyroxene) is in agreement with the bulk REE abundance (Figure 6). The consistency suggests that the REE evolution during crystallization of NWA 12241 occurred in a closed system in terms of REEs, suggesting an intermediate source reservoir for NWA 12241. The similar REE patterns in the pyroxene equilibrium melts suggest progressive fractional crystallization (Figure 6), whereas the variable extents of negative Eu anomalies imply that pyroxene crystallized either prior to or simultaneously with plagioclase (Wadhwa et al., 1994). The decoupling between the abundance of major elements and REE in NWA 12241 is likely due to the excess presence of Mg-rich olivine, which is a significant

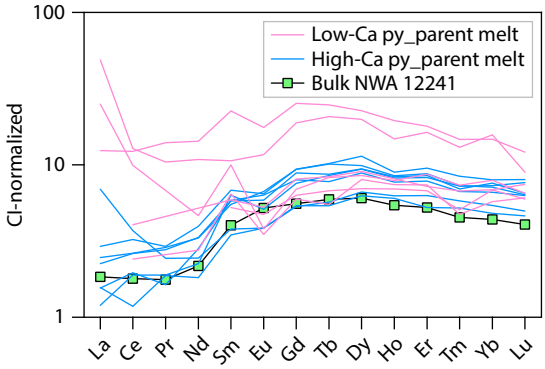

Figure 6. Calculated REE composition of melts in equilibrium with low-Ca pyroxene and high-Ca pyroxene.

contributor to the bulk MgO content but typically has low REE abundance. The excess of olivine is also supported by its quantitative textural characteristics with signs of accumulation.

The enrichment of La and Ce in melts in equilibrium with several pyroxene grains suggests selective LREE enrichment in pyroxene. These grains do not exhibit significantly higher contents of Ba (<7 ppm) and Sr (<5 ppm) compared with other grains, suggesting that terrestrial weathering has had a limited influence (Crozaz et al., 2003). Alternatively, the selective LREE enrichment in pyroxene could result from interaction with LREE-enriched fluids (McCubbin and Nekvasil, 2008). In either case, the effect is relatively subtle and not pervasive throughout the major phases. Therefore, the source material of NWA 12241 remains consistent with an intermediate signature, which is further supported by the measured ε_{Nd} and ε_{Hf} values of NWA 12241 (Lapen et al., 2019).

The intermediate source reservoirs could result from the mixing of depleted and enriched end-members, with the mixing potentially occurring between magmas, source mantle materials, crustal materials, or a combination thereof (Herd et al., 2002; Symes et al., 2008). Major and trace element compositions indicate that mixing between a depleted end-member chemically similar to Yamato 980459 with an enriched end-member chemically similar to NWA 1068 could explain the chemical variations of most shergottites (Treiman and Filiberto, 2015). Similarly, the chemical composition of the parent melt in NWA 12241 that formed during the early stage can be explained by mixing of a fractionated depleted component with a small amount of enriched component (Figures 7a–7b). Moreover, the relatively low Ni (310–487 ppm) and Co (107–112 ppm) contents of olivine in NWA 12241 indicate processes involving fractionation (Howarth and Udry, 2017). Given the in-depth origin of these pyroxenes and the intermediate chemical signature of equilibrium melts, the mixing process likely occurred at depths prior to magma ascent.

4.4 Emplacement History

Crystal distribution analysis allows for the quantitative evaluation of crystallization kinetics and the dynamics of igneous rocks, such as nucleation density, growth rates, and the accumulation or loss of crystals during crystallization (Marsh, 1988; Lentze and McSween, 2000; Basu Sarbadhikari et al., 2009). The downturns in the smallest size bins of the CSD profiles indicate processes such as resorption, fractionation, or annealing of early-formed olivine and pyroxene phenocrysts (Lentze and McSween, 2000). The touching framework of olivine suggests agglomeration, which could be related to heterogeneous nucleation, remobilization of cumulate mushes, or crystal settling (Jerram et al., 2003).

Given the similarities in textural observations and the in-depth origin of many pyroxenes in NWA 12241, the CSD results were compared with those of poikilitic and gabbroic shergottites to further quantitively evaluate the similarities in crystallization conditions. The CSD parameters for olivine in NWA 12241 are comparable to those of poikilitic shergottites, with the spatial distribution pattern most similar to that of the enriched poikilitic NWA 11043 and the intermediate ALHA 77005 (Figure 3a and 3c; Rahib et al., 2019). The relatively steeper CSD slope and smaller intercept of olivine larger than 0.1 mm in NWA 12241 compared with other poikilitic shergottites follows a trend of textural coarsening, indicating a similar process of crystal settling (Higgins, 2011; Rahib et al., 2019). In addition, the CSD slope of olivine grains with sizes greater than 0.1 mm corresponds to a relatively longer residence time of 149 Earth days, with a given growth rate

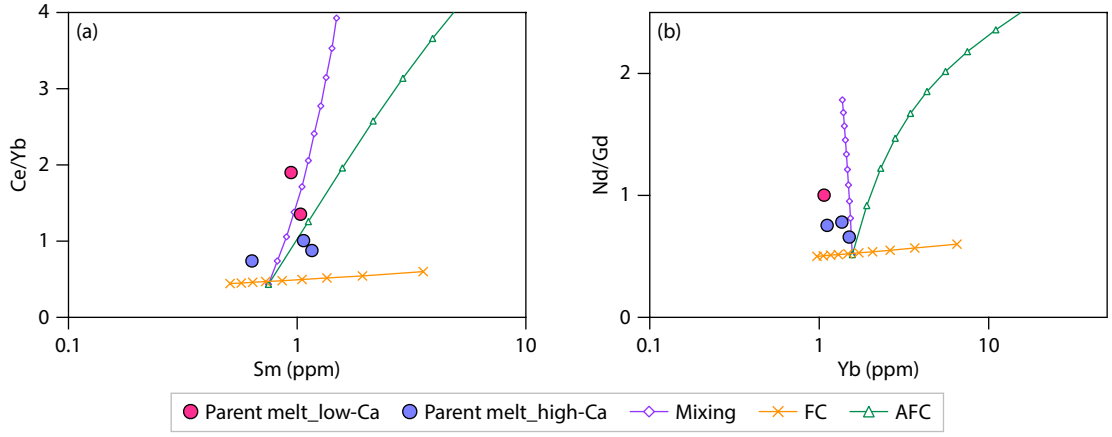

Figure 7. Parent melt compositions in the early stage compared with chemical variations resulting from processes of mixing, fractional crystallization (FC), and assimilation and fractional crystallization (AFC). (a) Ce/Yb versus Sm; (b) Nd/Gd versus Yb. The chemical evolution paths of FC began with the composition of Yamato 980459, whereas those of mixing and AFC started from a fractionated Yamato 980459.

of 3.1 × 10^{-8} mm/s (Basu Sarbadhikari et al., 2009). The CSD slope of pyroxene in NWA 12241 is slightly steeper than that of the enriched gabbroic NWA 13581 with a larger intercept (Figure 3b), indicating a higher nucleation density and a faster cooling rate compared with NWA 13581 (Wu YH et al., 2023). However, it is similar to that of the enriched gabbroic NWA 6963 (Filiberto et al., 2018).

Although small differences exist, these broad similarities suggest that NWA 12241 has a cumulate origin and underwent an emplacement process similar to those of poikilitic and gabbroic shergottites (Howarth et al., 2014; Filiberto et al., 2018; Rahib et al., 2019). This process likely involved initial ponding and crystallization under relatively reduced conditions at depth within a staging chamber, followed by a second stage of magma upwelling, emplacement, and crystallization with entrained crystals (Howarth et al., 2014; Combs et al., 2019; Rahib et al., 2019). Notably, the second stage of NWA 12241 is characterized by a greater accumulation of intermediate-sized olivine cumulates and a comparatively slower crystallization rate. This finding is supported by the relatively larger average grain size and longer residence time of olivine in NWA 12241 compared with most poikilitic shergottites (Rahib et al., 2019). The absence of rapid-growth olivine is consistent with a process of extended equilibrium growth (Eckley et al., 2024).

4.5 Crystallization Dynamics and Petrogenetic Links Among Intrusive Shergottites

The differences in the occurrence and morphology of poikilitic textures in poikilitic and gabbroic shergottites are influenced by various conditions, including growth rate, dissolution, and chemical equilibration during reaction and replacement (Hunter, 1996; Barnes et al., 2021). Experimental studies suggest that an extended intermediate temperature period, following the crystallization of orthopyroxene but prior to the crystallization of clinopyroxene and plagioclase, could enhance reactive crystallization, resulting in the formation of poikilitic textures in shergottites (Miura and Liang, 2020). Notably, interlayered lithologies at various scales could form as a result of heterogeneous mixing during mechanical settling of oikocrysts in a flowing crystal mush (Barnes et al., 2016). Such processes are prevalent in terrestrial mafic intrusions, which exhibit vertical variations in lithology, mineral proportion, and composition (Boorman et al., 2004; Barnes et al., 2021). These processes may also apply to the close association of poikilitic and gabbroic shergottites with different petrological signatures (Rahib et al., 2019; Wu YH et al., 2023; Benaroya et al., 2024). Moreover, fractional crystallization, mixing, assimilation, or a combination thereof would further enhance the chemical variability across different lithological subtypes (Filiberto et al., 2012; Treiman and Filiberto, 2015; Barnes et al., 2016).

A compositionally and density-stratified igneous terrain has been identified in Jezero crater on Mars through data acquired by the Perseverance rover (Wiens et al., 2022), providing evidence for the presence of cogenetic magmatic suites with different lithologies on Mars. The magma body exhibits plagioclase enrichment at a shallower depth and an olivine-rich unit at the lowest formation in the crater floor, known as the Séítah formation (Wiens et al., 2022). Outcrops of the olivine cumulates in the Séítah formation exhibit a poikilitic texture, which is suggested to have formed through settling and enrichment of olivine during multistage cooling of a thick magma body (Liu Y et al., 2022). Moreover, the bulk major element compositions of the Séítah formation fall within the range of poikilitic shergottites (Wiens et al., 2022). Although the exhumation history of Jezero crater is not fully constrained, the presence of lithologies similar to some rocks observed at Gusev crater and in Martian meteorites (e.g., poikilitic shergottites and a few chassignites) suggests the pervasive occurrence of cumulate rocks with lithological diversities (Beyssac et al., 2023).

Notably, fluid interaction products observed in NWA 12241 are similar to those in intermediate NWA 6234, enriched gabbroic NWA 13581, and enriched poikilitic NWA 7755, characterized by irregular boundaries and vermicular iron oxide phases in phosphates (Gross et al., 2013a; Howarth et al., 2015; Wu YH et al., 2024). This finding implies that although different igneous bodies of shergottites are required to account for various observations, such as the broad range of crystallization ages (Nyquist et al., 2001), the variable isotopic compositions of source reservoirs (Armytage et al., 2018; Combs et al., 2019; Wu YH et al., 2023), and systematic differences in olivine morphologies (Eckley et al., 2024), common processes link their formation, emplacement, and alteration histories.

5. Summary

Petrological and geochemical analyses indicate that NWA 12241 is an intermediate gabbroic shergottite with a cumulate origin. Its mineral composition, as well as bulk major and trace element abundances, are largely similar to those of currently identified intermediate poikilitic shergottites. The parent melt REE composition of NWA 12241 is consistent with an intermediate signature, likely resulting from the mixing of enriched and depleted components and involving fractional crystallization prior to magma ascent. Although intermediate and enriched shergottites likely formed in different magmatic bodies, their quantitative textural characteristics reveal a close relationship between NWA 12241 and both intermediate and enriched gabbroic and poikilitic shergottites. Their similarities suggest similar emplacement processes involving ponding and crystallization in a deep staging chamber, followed by subsequent crystallization during magma ascent and emplacement (Howarth et al., 2014; Combs et al., 2019; Rahib et al., 2019). Variations in crystallization dynamics within magma chambers and magmatic plumbing systems, such as melt replenishment, duration, and temperature in staging chambers, and the flow of crystal mush further lead to petrological and compositional stratigraphic variations among samples of different petrological subtypes (Howarth et al., 2014; Barnes et al., 2016; Cashman et al., 2017; Miura and Liang Y, 2020).

Our study highlights the lithological diversity of Martian intrusive meteorites. On the basis of current observations, future collections are expected to yield intrusive samples with a greater diversity of petrological and mineralogical characteristics, yet with close petrogenetic associations. These may include variations in olivine abundance, the presence of poikilitic pyroxene, differences in grain sizes, and variations in mineral chemistry, regardless of

whether they are derived from the same magma body or from distinct source regions. Moreover, the presence of similar secondary products (e.g., iron oxide in phosphates) in shergottites further indicates the presence of similar and pervasive aqueous alteration among different shergottites. In conclusion, the similarities in mineral chemistry across various shergottites suggest the existence of multiple magma chambers at the crust–mantle boundary, with compositions ranging from depleted to enriched. Moreover, the formation history of NWA 12241 and similar crystallization dynamics with other shergottites indicate that subsequent magmatic differentiation and cooling conditions at shallow levels are crucial processes leading to textural and compositional variations among samples of different petrological subtypes.

Acknowledgments

This work is supported by the National Natural Science Foundation of China (Nos. 42473049, 42241108, and 42273040), the Guangdong Basic and Applied Basic Research Foundation (No. 2024A1515011311), and the Open Project for Innovative Platform of Meteoritical Research, Shanghai Science and Technology Museum.

References

Armytage, R. M. G., Debaille, V., Brandon, A. D., and Agee, C. B. (2018). A complex history of silicate differentiation of Mars from Nd and Hf isotopes in crustal breccia NWA 7034. *Earth Planet. Sci. Lett.*, *502*, 274–283. https://doi.org/10.1016/j.epsl.2018.08.013

Balta, J. B., Sanborn, M., McSween, H. Y., Jr., and Wadhwa, M. (2013). Magmatic history and parental melt composition of olivine-phyric shergottite LAR 06319: Importance of magmatic degassing and olivine antecrysts in Martian magmatism. *Meteorit. Planet. Sci.*, *48*(8), 1359–1382. https://doi.org/10.1111/maps.12140

Barnes, S. J., Mole, D. R., Le Vaillant, M., Campbell, M. J., Verrall, M. R., Roberts, M. P., and Evans, N. J. (2016). Poikilitic textures, heteradcumulates and zoned orthopyroxenes in the Ntaka Ultramafic Complex, Tanzania: Implications for crystallization mechanisms of oikocrysts. *J. Petrol.*, *57*(6), 1171–1198. https://doi.org/10.1093/petrology/egw036

Barnes, S. J., Latypov, R., Chistyakova, S., Godel, B., and Schoneveld, L. E. (2021). Idiomorphic oikocrysts of clinopyroxene produced by a peritectic reaction within a solidification front of the Bushveld Complex. *Contrib. Mineral. Petrol.*, *176*(1), 5. https://doi.org/10.1007/s00410-020-01747-4

Barrat, J. A., Blichert-Toft, J., Nesbitt, R. W., and Keller, F. (2001). Bulk chemistry of Saharan shergottite Dar al Gani 476. *Meteorit. Planet. Sci.*, *36*(1), 23–29. https://doi.org/10.1111/j.1945-5100.2001.tb01807.x

Barrat, J. A., Jambon, A., Bohn, M., Gillet, P. H., Sautter, V., Göpel, C., Lesourd, M., and Keller, F. (2002). Petrology and chemistry of the picritic shergottite North West Africa 1068 (NWA 1068). *Geochim. Cosmochim. Acta*, *66*(19), 3505–3518. https://doi.org/10.1016/S0016-7037(02)00934-1

Basu Sarbadhikari, A., Day, J. M. D., Liu, Y., Rumble, D., III, and Taylor, L. A. (2009). Petrogenesis of olivine-phyric shergottite Larkman Nunatak 06319: Implications for enriched components in Martian basalts. *Geochim. Cosmochim. Acta*, *73*(7), 2190–2214. https://doi.org/10.1016/j.gca.2009.01.012

Bédard, J. H. (2010). Parameterization of the Fe=Mg exchange coefficient (Kd) between clinopyroxene and silicate melts. *Chem. Geol.*, *274*(3-4), 169–176. https://doi.org/10.1016/j.chemgeo.2010.04.003

Benaroya, S., Gross, J., Burger, P., Righter, M., Lapen, T. J., and Eckley, S. (2024). Petrogenesis of a new type of intrusive shergottite: Olivine-gabbro Northwest Africa 13227. *Geochim. Cosmochim. Acta*, *370*, 41–65. https://doi.org/10.1016/j.gca.2024.02.004

Beyssac, O., Forni, O., Cousin, A., Udry, A., Kah, L. C., Mandon, L., Clavé, O. E., Liu, Y., Poulet, F., … The SuperCam Team. (2023). Petrological traverse of the olivine cumulate Séítah formation at Jezero crater, Mars: A perspective from SuperCam onboard perseverance. *J. Geophys. Res.: Planets*, *128*(7), e2022JE007638. https://doi.org/10.1029/2022JE007638

Boorman, S., Boudreau, A., and Kruger, F. J. (2004). The lower zone–critical zone transition of the Bushveld Complex: A quantitative textural study. *J. Petrol.*, *45*(6), 1209–1235. https://doi.org/10.1093/petrology/egh011

Brandon, A. D., Puchtel, I. S., Walker, R. J., Day, J. M. D., Irving, A. J., and Taylor, L. A. (2012). Evolution of the Martian mantle inferred from the ^{187}Re–^{187}Os isotope and highly siderophile element abundance systematics of shergottite meteorites. *Geochim. Cosmochim. Acta*, *76*, 206–235. https://doi.org/10.1016/j.gca.2011.09.047

Cashman, K. V., Sparks, R. S. J., and Blundy, J. D. (2017). Vertically extensive and unstable magmatic systems: A unified view of igneous processes. *Science*, *355*(6331), eaag3055. https://doi.org/10.1126/science.aag3055

Castle, N., and Herd, C. D. K. (2017). Experimental petrology of the Tissint meteorite: Redox estimates, crystallization curves, and evaluation of petrogenetic models. *Meteorit. Planet. Sci.*, *52*(1), 125–146. https://doi.org/10.1111/maps.12739

Combs, L. M., Udry, A., Howarth, G. H., Righter, M., Lapen, T. J., Gross, J., Ross, D. K., Rahib, R. R., and Day, J. M. D. (2019). Petrology of the enriched poikilitic shergottite Northwest Africa 10169: Insight into the Martian interior. *Geochim. Cosmochim. Acta*, *266*, 435–462. https://doi.org/10.1016/j.gca.2019.07.001

Crozaz, G., Floss, C., and Wadhwa, M. (2003). Chemical alteration and REE mobilization in meteorites from hot and cold deserts. *Geochim. Cosmochim. Acta*, *67*(24), 4727–4741. https://doi.org/10.1016/j.gca.2003.08.008

Day, J. M. D., Tait, K. T., Udry, A., Moynier, F., Liu, Y., and Neal, C. R. (2018). Martian magmatism from plume metasomatized mantle. *Nat. Commun.*, *9*(1), 4799. https://doi.org/10.1038/s41467-018-07191-0

Eckley, S. A., Ketcham, R. A., Liu, Y., Udry, A., and Gross, J. (2024). New olivine morphologies in shergottites reveal complex thermal histories of Martian magmas. *Geochim. Cosmochim. Acta*, *373*, 197–210. https://doi.org/10.1016/j.gca.2024.04.006

Ennis, M. E., and McSween, H. Y., Jr. (2014). Crystallization kinetics of olivine-phyric shergottites. *Meteorit. Planet. Sci.*, *49*(8), 1440–1455. https://doi.org/10.1111/maps.12349

Filiberto, J., Musselwhite, D. S., Gross, J., Burgess, K., Le, L. A., and Treiman, A. H. (2010). Experimental petrology, crystallization history, and parental magma characteristics of olivine-phyric shergottite NWA 1068: Implications for the petrogenesis of "enriched" olivine-phyric shergottites. *Meteorit. Planet. Sci.*, *45*(8), 1258–1270. https://doi.org/10.1111/j.1945-5100.2010.01080.x

Filiberto, J., and Dasgupta, R. (2011). Fe^{2+}-mg partitioning between olivine and basaltic melts: Applications to genesis of olivine-phyric shergottites and conditions of melting in the Martian interior. *Earth Planet. Sci. Lett.*, *304*(3-4), 527–537. https://doi.org/10.1016/j.epsl.2011.02.029

Filiberto, J., Chin, E., Day, J. M. D., Franchi, I. A., Greenwood, R. C., Gross, J., Penniston-Dorland, S. C., Schwenzer, S. P., and Treiman, A. H. (2012). Geochemistry of intermediate olivine-phyric shergottite Northwest Africa 6234, with similarities to basaltic shergottite Northwest Africa 480 and olivine-phyric shergottite Northwest Africa 2990. *Meteorit. Planet. Sci.*, *47*(8), 1256–1273. https://doi.org/10.1111/j.1945-5100.2012.01382.x

Filiberto, J., Gross, J., Trela, J., and Ferré, E. C. (2014). Gabbroic shergottite Northwest Africa 6963: An intrusive sample of Mars. *Am. Mineral.*, *99*(4), 601–606. https://doi.org/10.2138/am.2014.4638

Filiberto, J., and Dasgupta, R. (2015). Constraints on the depth and thermal vigor of melting in the Martian mantle. *J. Geophys. Res.: Planets*, *120*(1), 109–122. https://doi.org/10.1002/2014JE004745

Filiberto, J., Gross, J., Udry, A., Trela, J., Wittmann, A., Cannon, K. M., Penniston-Dorland, S., Ash, R., Hamilton, V. E., … Ferré, E. C. (2018). Shergottite Northwest Africa 6963: A pyroxene-cumulate Martian gabbro. *J. Geophys. Res.: Planets*, *123*(7), 1823–1841. https://doi.org/10.1029/2018JE005635

Gattacceca, J., McCubbin, F. M., Bouvier, A., and Grossman, J. (2020). The Meteoritical Bulletin, No. *107*. *Meteorit. Planet. Sci.*, *55*(2), 460–462. https://doi.org/10.1111/maps.13440

Goodrich, C. A. (2002). Olivine-phyric Martian basalts: A new type of shergottite.

Meteorit. Planet. Sci., *37*(S12), B31–B34. https://doi.org/10.1111/j.1945-5100.2002.tb00901.x

Goodrich, C. A., Herd, C. D. K., and Taylor, L. A. (2003). Spinels and oxygen fugacity in olivine-phyric and lherzolitic shergottites. *Meteorit. Planet. Sci.*, *38*(12), 1773–1792. https://doi.org/10.1111/j.1945-5100.2003.tb00014.x

Gross, J., Filiberto, J., Herd, C. D. K., Daswani, M. M., Schwenzer, S. P., and Treiman, A. H. (2013a). Petrography, mineral chemistry, and crystallization history of olivine-phyric shergottite NWA 6234: A new melt composition. *Meteorit. Planet. Sci.*, *48*(5), 854–871. https://doi.org/10.1111/maps.12092

Gross, J., Filiberto, J., and Bell, A. S. (2013b). Water in the Martian interior: Evidence for terrestrial MORB mantle-like volatile contents from hydroxyl-rich apatite in olivine–phyric shergottite NWA 6234. *Earth Planet. Sci. Lett.*, *369–370*, 120–128. https://doi.org/10.1016/j.epsl.2013.03.016

Herd, C. D. K., Papike, J. J., and Brearley, A. J. (2001). Oxygen fugacity of Martian basalts from electron microprobe oxygen and TEM-EELS analyses of Fe-Ti oxides. *Am. Mineral.*, *86*(9), 1015–1024. https://doi.org/10.2138/am-2001-8-908

Herd, C. D. K., Borg, L. E., Jones, J. H., and Papike, J. J. (2002). Oxygen fugacity and geochemical variations in the Martian basalts: Implications for Martian basalt petrogenesis and the oxidation state of the upper mantle of Mars. *Geochim. Cosmochim. Acta*, *66*(11), 2025–2036. https://doi.org/10.1016/S0016-7037(02)00828-1

Herd, C. D. K. (2003). The oxygen fugacity of olivine-phyric Martian basalts and the components within the mantle and crust of Mars. *Meteorit. Planet. Sci.*, *38*(12), 1793–1805. https://doi.org/10.1111/j.1945-5100.2003.tb00015.x

Higgins, M. D. (2000). Measurement of crystal size distributions. *Am. Mineral.*, *85*(9), 1105–1116. https://doi.org/10.2138/am-2000-8-901

Higgins, M. D. (2011). Textural coarsening in igneous rocks. *Int. Geol. Rev.*, *53*(3-4), 354–376. https://doi.org/10.1080/00206814.2010.496177

Howarth, G. H., Pernet-Fisher, J. F., Balta, J. B., Barry, P. H., Bodnar, R. J., and Taylor, L. A. (2014). Two-stage polybaric formation of the new enriched, pyroxene-oikocrystic, lherzolitic shergottite, NWA 7397. *Meteorit. Planet. Sci.*, *49*(10), 1812–1830. https://doi.org/10.1111/maps.12357

Howarth, G. H., Pernet-Fisher, J. F., Bodnar, R. J., and Taylor, L. A. (2015). Evidence for the exsolution of Cl-rich fluids in Martian magmas: Apatite petrogenesis in the enriched lherzolitic shergottite Northwest Africa 7755. *Geochim. Cosmochim. Acta*, *166*, 234–248. https://doi.org/10.1016/j.gca.2015.06.031

Howarth, G. H., and Udry, A. (2017). Trace elements in olivine and the petrogenesis of the intermediate, olivine-phyric shergottite NWA 10170. *Meteorit. Planet. Sci.*, *52*(2), 391–409. https://doi.org/10.1111/maps.12799

Hui, H. J., Peslier, A. H., Lapen, T. J., Shafer, J. T., Brandon, A. D., and Irving, A. J. (2011). Petrogenesis of basaltic shergottite Northwest Africa 5298: Closed-system crystallization of an oxidized mafic melt. *Meteorit. Planet. Sci.*, *46*(9), 1313–1328. https://doi.org/10.1111/j.1945-5100.2011.01231.x

Hunter, R. H. (1996). Texture development in cumulate rocks. In R. G. Cawthorn (Ed.), *Developments in Petrology* (Vol. 15, pp. 77–101). Amsterdam: Elsevier. https://doi.org/10.1016/S0167-2894(96)80005-4

Irving, A. J., Kuehner, S. M., Herd, C. D. K., Gellissen, M., Rumble, D., III, Lapen, T. J., Ralew, S., and Altmann, M. (2010). Olivine-bearing diabasic shergottite Northwest Africa 5990: Petrology and composition of a new type of depleted Martian igneous rock. In *41st Lunar and Planetary Science Conference*. The Woodlands, Texas: Lunar and Planetary Institute. 1833.

Irving, A. J., Bunch, T. E., Kuehner, S. M., Herd, C. D. K., Gellissen, M., Lapen, T. J., Rumble, D., and Pitt, D. (2011). Petrologic, elemental and isotopic characterization of shock-melted, enriched ultramafic poikilitic shergottite Northwest Africa 6342. In *42nd Lunar and Planetary Science Conference*. The Woodlands, Texas: Lunar and Planetary Institute. 1612.

Irving, A. J., Kuehner, S. M., Carpenter, P. K., Moser, D. E., Barker, I., Righter, M., Lapen, T. J., Weimer, D., Busemann, H., Ziegler, K. and Hoefnagels, B. (2018). Petrologic, isotopic and elemental characterization of shock-melted intermediate olivine gabbroic shergottite Northwest Africa 11509. In *49th Lunar and Planetary Science Conference*. The Woodlands, Texas: Lunar and Planetary Institute. 2279.

Jambon, A., Barrat, J. A., Sautter, V., Gillet, P., Göpel, C., Javoy, M., Joron, J. L., and Lesourd, M. (2002). The basaltic shergottite Northwest Africa 856: Petrology and chemistry. *Meteorit. Planet. Sci.*, *37*(9), 1147–1164. https://doi.org/10.1111/j.1945-5100.2002.tb00885.x

Jerram, D. A., Cheadle, M. J., Hunter, R. H., and Elliott, M. T. (1996). The spatial distribution of grains and crystals in rocks. *Contrib. Mineral. Petrol.*, *125*(1), 60–74. https://doi.org/10.1007/s004100050206

Jerram, D. A., Cheadle, M. J., and Philpotts, A. R. (2003). Quantifying the building blocks of igneous rocks: Are clustered crystal frameworks the foundation?. *J. Petrol.*, *44*(11), 2033–2051. https://doi.org/10.1093/petrology/egg069

Kring, D. A., Gleason, J. D., Swindle, T. D., Nishiizumi, K., Caffee, M. W., Hill, D. H., Jull, A. J. T., and Boynton, W. V. (2003). Composition of the first bulk melt sample from a volcanic region of Mars: Queen Alexandra Range 94201. *Meteorit. Planet. Sci.*, *38*(12), 1833–1848. https://doi.org/10.1111/j.1945-5100.2003.tb00018.x

Lapen, T. J., Righter, M., Andreasen, R., Irving, A. J., Satkoski, A. M., Beard, B. L., Nishiizumi, K., Jull, A. J. T., and Caffee, M. W. (2017). Two billion years of magmatism recorded from a single Mars meteorite ejection site. *Sci. Adv.*, *3*(2), e1600922. https://doi.org/10.1126/sciadv.1600922

Lapen, T. J., Righter, M., Irving, A. J., Kuehner, S. M., Carpenter, P. K., Gessler, N., Aid, M., Aaronson, A., Arjdal, M., and Hoefnagels, B. (2019). Martian meteorite rain: Petrology, elemental and isotopic composition of ten recently recovered shergottites. In *50th Lunar and Planetary Science Conference*. The Woodlands, Texas: Lunar and Planetary Institute. 2605.

Lentze, R. C. F., and McSween, H. Y., Jr. (2000). Crystallization of the basaltic shergottites: Insights from crystal size distribution (CSD) analysis of pyroxenes. *Meteorit. Planet. Sci.*, *35*(5), 919–927. https://doi.org/10.1111/j.1945-5100.2000.tb01481.x

Liu, Y., Tice, M. M., Schmidt, M. E., Treiman, A. H., Kizovski, T. V., Hurowitz, J. A., Allwood, A. C., Henneke, J., Pedersen, D. A. K., … Zorzano, M. P. (2022). An olivine cumulate outcrop on the floor of Jezero crater, Mars. *Science*, *377*(6614), 1513–1519. https://doi.org/10.1126/science.abo2756

Lodders, K. (1998). A survey of shergottite, nakhlite and chassigny meteorites whole-rock compositions. *Meteorit. Planet. Sci.*, *33*(S4), A183–A190. https://doi.org/10.1111/j.1945-5100.1998.tb01331.x

Marsh, B. D. (1988). Crystal size distribution (CSD) in rocks and the kinetics and dynamics of crystallization. *Contrib. Mineral. Petrol.*, *99*(3), 277–291. https://doi.org/10.1007/BF003753620

McCubbin, F. M., and Nekvasil, H. (2008). Maskelynite-hosted apatite in the Chassigny meteorite: Insights into late-stage magmatic volatile evolution in Martian magmas. *Am. Mineral.*, *93*(4), 676–684. https://doi.org/10.2138/am.2008.2558

McSween, H. Y., Jr., and Treiman, A. H. (1998). Martian meteorites. In J. J. Papike (Ed.), *Planetary Materials* (pp. 6-1–6-54). Washington, DC: Mineralogical Society of America.

Miura, J. K., and Liang, Y. (2020). A reactive crystallization model for the formation of poikilitic shergottite meteorites. In *51st Lunar and Planetary Science Conference*. The Woodlands, Texas: Lunar and Planetary Science Institute. 2477.

Morgan, D. J., and Jerram, D. A. (2006). On estimating crystal shape for crystal size distribution analysis. *J. Volcanol. Geotherm. Res.*, *154*(1-2), 1–7. https://doi.org/10.1016/j.jvolgeores.2005.09.016

Nekvasil, H., Dondolini, A., Horn, J., Filiberto, J., Long, H., and Lindsley, D. H. (2004). The origin and evolution of silica-saturated alkalic suites: An experimental study. *J. Petrol.*, *45*(4), 693–721. https://doi.org/10.1093/petrology/egg103

Nicklas, R. W., Day, J. M. D., Vaci, Z., Udry, A., Liu, Y., and Tait, K. T. (2021). Uniform oxygen fugacity of shergottite mantle sources and an oxidized martian lithosphere. *Earth Planet. Sci. Lett.*, *564*, 116876. https://doi.org/10.1016/j.epsl.2021.116876

Nikolaev, G. S., Ariskin, A. A., Barmina, G. S., Nazarov, M. A., and Almeev, R. R. (2016). Test of the Ballhaus–Berry–Green *Ol–Opx–Sp* oxybarometer and calibration of a new equation for estimating the redox state of melts saturated with olivine and spinel. *Geochem. Int.*, *54*(4), 301–320. https://doi.org/10.1134/S0016702916040078

Nyquist, L. E., Bogard, D. D., Shih, C. Y., Greshake, A., Stöffler, D., and Eugster, O. (2001). Ages and geologic histories of Martian meteorites. *Space Sci. Rev.*, *96*(1), 105–164. https://doi.org/10.1023/A:1011993105172

Papike, J. J., Karner, J. M., Shearer, C. K., and Burger, P. V. (2009). Silicate mineralogy of Martian meteorites. *Geochim. Cosmochim. Acta*, *73*(24), 7443–7485. https://doi.org/10.1016/j.gca.2009.09.008

Peslier, A. H., Hnatyshin, D., Herd, C. D. K., Walton, E. L., Brandon, A. D., Lapen, T. J., and Shafer, J. T. (2010). Crystallization, melt inclusion, and redox history of a Martian meteorite: Olivine-phyric shergottite Larkman Nunatak 06319. *Geochim. Cosmochim. Acta*, *74*(15), 4543–4576. https://doi.org/10.1016/j.gca.2010.05.002

Rahib, R. R., Udry, A., Howarth, G. H., Gross, J., Paquet, M., Combs, L. M., Laczniak, D. L., and Day, J. M. D. (2019). Mantle source to near-surface emplacement of enriched and intermediate poikilitic shergottites in Mars. *Geochim. Cosmochim. Acta*, *266*, 463–496. https://doi.org/10.1016/j.gca.2019.07.034

Shafer, J. T., Brandon, A. D., Lapen, T. J., Righter, M., Peslier, A. H., and Beard, B. L. (2010). Trace element systematics and ^{147}Sm–^{143}Nd and ^{176}Lu–^{176}Hf ages of Larkman Nunatak 06319: Closed-system fractional crystallization of an enriched shergottite magma. *Geochim. Cosmochim. Acta*, *74*(24), 7307–7328. https://doi.org/10.1016/j.gca.2010.09.009

Shirai, N., and Ebihara, M. (2004). Chemical characteristics of a Martian meteorite, Yamato 980459. *Antarct. Meteorite Res.*, *17*, 55–67.

Sun, C. G., and Liang, Y. (2012). Distribution of REE between clinopyroxene and basaltic melt along a mantle adiabat: Effects of major element composition, water, and temperature. *Contrib. Mineral. Petrol.*, *163*(5), 807–823. https://doi.org/10.1007/s00410-011-0700-x

Sun, C. G., and Liang, Y. (2013). Distribution of REE and HFSE between low-Ca pyroxene and lunar picritic melts around multiple saturation points. *Geochim. Cosmochim. Acta*, *119*, 340–358. https://doi.org/10.1016/j.gca.2013.05.036

Symes, S. J. K., Borg, L. E., Shearer, C. K., and Irving, A. J. (2008). The age of the Martian meteorite Northwest Africa 1195 and the differentiation history of the shergottites. *Geochim. Cosmochim. Acta*, *72*(6), 1696–1710. https://doi.org/10.1016/j.gca.2007.12.022

Takenouchi, A., Yamaguchi, A., Mikouchi, T., Greenwood, R., and Yamazaki, S. (2023). Petrology and shock history of the first depleted-like poikilitic shergottite Asuka 12325. *Meteorit. Planet. Sci.*, *58*(10), 1406–1428. https://doi.org/10.1111/maps.14073

Thompson, J. M., Meffre, S., and Danyushevsky, L. (2018). Impact of air, laser pulse width and fluence on U-Pb dating of zircons by LA-ICPMS. *J. Anal. At. Spectrom.*, *33*(2), 221–230. https://doi.org/10.1039/C7JA00357A

Treiman, A. H., and Filiberto, J. (2015). Geochemical diversity of shergottite basalts: Mixing and fractionation, and their relation to Mars surface basalts. *Meteorit. Planet. Sci.*, *50*(4), 632–648. https://doi.org/10.1111/maps.12363

Udry, A., Howarth, G. H., Lapen, T. J., and Righter, M. (2017). Petrogenesis of the NWA 7320 enriched Martian gabbroic shergottite: Insight into the Martian crust. *Geochim. Cosmochim. Acta*, *204*, 1–18. https://doi.org/10.1016/j.gca.2017.01.032

Udry, A., and Day, J. M. D. (2018). 1.34 billion-year-old magmatism on Mars evaluated from the co-genetic nakhlite and chassignite meteorites. *Geochim. Cosmochim. Acta*, *238*, 292–315. https://doi.org/10.1016/j.gca.2018.07.006

Udry, A., Howarth, G. H., Herd, C. D. K., Day, J. M. D., Lapen, T. J., and Filiberto, J. (2020). What Martian meteorites reveal about the interior and surface of Mars. *J. Geophys. Res.: Planets*, *125*(12), e2020JE006523. https://doi.org/10.1029/2020JE006523

Van Niekerk, D., Goodrich, C. A., Taylor, G. J., and Keil, K. (2007). Characterization of the lithological contact in the shergottite EETA79001—A record of igneous differentiation processes on Mars. *Meteorit. Planet. Sci.*, *42*(10), 1751–1762. https://doi.org/10.1111/j.1945-5100.2007.tb00535.x

Wadhwa, M., McSween, H. Y., Jr., and Crozaz, G. (1994). Petrogenesis of shergottite meteorites inferred from minor and trace element microdistributions. *Geochim. Cosmochim. Acta*, *58*(19), 4213–4229. https://doi.org/10.1016/0016-7037(94)90274-7

Wieler, R., Huber, L., Busemann, H., Seiler, S., Leya, I., Maden, C., Masarik, J., Meier, M. M. M., Nagao, K., … Irving, A. J. (2016). Noble gases in 18 Martian meteorites and angrite Northwest Africa 7812—Exposure ages, trapped gases, and a re-evaluation of the evidence for solar cosmic ray-produced neon in shergottites and other achondrites. *Meteorit. Planet. Sci.*, *51*(2), 407–428. https://doi.org/10.1111/maps.12600

Wiens, R. C., Udry, A., Beyssac, O., Quantin-Nataf, C., Mangold, N., Cousin, A., Mandon, L., Bosak, T., Forni, O., … The SuperCam Team. (2022). Compositionally and density stratified igneous terrain in Jezero crater, Mars. *Sci. Adv.*, *8*(34), eabo3399. https://doi.org/10.1126/sciadv.abo3399

Wu, Y. H., Xiao, Z. Y., Wu, Y. X., Pan, L. L., Yan, P., Liao, S. Y., Pan, Q., Li, S. L., Li, Y., and Hsu, W. B. (2024). Hydrothermal fluid activity on Mars recorded in phosphates of the gabbroic shergottite Northwest Africa 13581. *J. Geophys. Res.: Planets*, *129*(10), e2024JE008412. https://doi.org/10.1029/2024JE008412

Wu, Y. H., Hsu, W. B., Liao, S. Y., Xiao, Z. Y., Che, X. C., Pan, L. L., Li, Y., and Li, S. L. (2023). Petrology and mineralogy of the Martian olivine gabbroic shergottite Northwest Africa 13581: Insights into the enriched Martian mantle source. *Geochim. Cosmochim. Acta*, *358*, 108–125. https://doi.org/10.1016/j.gca.2023.08.003

Yao, L. J., Sun, C. G., and Liang, Y. (2012). A parameterized model for REE distribution between low-Ca pyroxene and basaltic melts with applications to REE partitioning in low-Ca pyroxene along a mantle adiabat and during pyroxenite-derived melt and peridotite interaction. *Contrib. Mineral. Petrol.*, *164*(2), 261–280. https://doi.org/10.1007/s00410-012-0737-5

Zuber, M. T., Solomon, S. C., Phillips, R. J., Smith, D. E., Tyler, G. L., Aharonson, O., Balmino, G., Banerdt, W. B., Head, J. W., … Zhong, S. J. (2000). Internal structure and early thermal evolution of Mars from Mars Global Surveyor topography and gravity. *Science*, *287*(5459), 1788–1793. https://doi.org/10.1126/science.287.5459.1788